



Cite this: *J. Mater. Chem. A*, 2022, 10, 24519

# Self-assembly of a heterogeneous microreactor with carbon dots embedded in Ti-MOF derived $\text{ZnIn}_2\text{S}_4/\text{TiO}_2$ microcapsules for efficient $\text{CO}_2$ photoreduction†

Dongxue Wu,<sup>a</sup> Qian Liang,<sup>ID</sup> \*<sup>a</sup> Honglin Si,<sup>b</sup> Xiong Yan,<sup>b</sup> Hui Huang,<sup>ID</sup> <sup>b</sup>  
Zhongyu Li<sup>ID</sup> \*<sup>a</sup> and Zhenhui Kang<sup>ID</sup> \*<sup>bcd</sup>

The assembly of the heterogeneous microreactor is a promising approach for  $\text{CO}_2$  photoreduction attributed to its abundant microchannel, intimate contact, high exposed surface area, and favorable heat-mass transfer. Herein, we developed a metal-organic framework (MOF) derived *in situ* transformation strategy to construct a carbon dot (CD)-decorated  $\text{ZnIn}_2\text{S}_4/\text{TiO}_2$  (CDs/ZIS/ $\text{TiO}_2$ ) microreactor. Taking advantages of this hierarchical structure, the CDs/ $\text{ZnIn}_2\text{S}_4/\text{TiO}_2$  microreactor exhibits significantly enhanced photocatalytic  $\text{CO}_2$  reduction activity with a  $\text{CH}_4$  yield of  $14.9 \mu\text{mol g}^{-1} \text{h}^{-1}$  and  $\text{CH}_4$  selectivity of 75.6% in the absence of a sacrificial agent, where the electron consumption rate ( $R_{\text{electron}}$ ) of  $157.6 \mu\text{mol g}^{-1} \text{h}^{-1}$  is 1.9 and 18.3 times higher than those of ZIS(60)/ $\text{TiO}_2$  and bare  $\text{ZnIn}_2\text{S}_4$ , respectively. The combination of transient photo-induced voltage (TPV), *in situ* Fourier transform infrared and electron spin resonance (ESR) spectra illustrate the photocatalytic mechanism and the effect of CDs on the electron transfer behavior. This work emphasizes a facile technique for developing a CD-based microreactor to achieve high-efficiency photocatalytic  $\text{CO}_2$  reduction performance.

Received 14th September 2022  
Accepted 27th October 2022

DOI: 10.1039/d2ta07217c

rsc.li/materials-a

## 1. Introduction

Solar-driven  $\text{CO}_2$  reduction is an attractive and efficient way to directly convert  $\text{CO}_2$  into fuels and high value-added products, such as CO,  $\text{CH}_4$ ,  $\text{CH}_3\text{OH}$ , and  $\text{C}_2\text{H}_4$ .<sup>1–3</sup> Among the C1 products,  $\text{CH}_4$  as a popular and clean energy source is one of the most important fuels, and so far, enormous efforts have been focused on the construction of semiconductor catalysts to improve the yield and selectivity of  $\text{CH}_4$ .<sup>4–7</sup> Ternary chalcogenide  $\text{ZnIn}_2\text{S}_4$  with a layered structure can convert  $\text{CO}_2$  into useful fuels (e.g., CO,  $\text{H}_2$ ,  $\text{CH}_4$ ) with considerable performance due to their appropriate band gap structure and great visible-light absorption ability.<sup>8</sup> Although  $\text{ZnIn}_2\text{S}_4$ -based catalysts present a high  $\text{CO}_2$ -to-(CO +  $\text{H}_2$ ) conversion efficiency, the photocatalytic

activity and selectivity of  $\text{CH}_4$  in their gas products are insufficient.<sup>9–11</sup>

On account of the enhancement of  $\text{CH}_4$  production, the development of a  $\text{ZnIn}_2\text{S}_4$ -based heterogeneous microreactor can be considered an effective strategy due to its high surface-to-volume ratio, abundant microchannels, and favorable heat-mass transfer. This heterogeneous microreactor can strengthen the electron trapping ability, and thus requires more electrons and protons to generate  $\text{CH}_4$ . Metal-organic frameworks (MOFs) with fascinating topology, large pore volume, and chemical adjustability provide an excellent platform to fabricate the semiconductors with a microcapsule structure<sup>12,13</sup> including metal oxides,<sup>14</sup> metal sulfides,<sup>15</sup> layered double hydroxides (LDHs) by using ion-exchange or solvothermal method,<sup>16</sup> which enables the encapsulation of numerous nanoparticles or nanosheets on the capsules. For instance, Bibi *et al.* found that thioacetamide (TAA) can decompose MIL-125 to form  $\text{TiO}_2/\text{CdS}$  capsules after the post-solvothermal method, which exhibited enhanced photocatalytic activity.<sup>17</sup> MOF-derived microcapsules as a crucial part of the microreactor can provide high porosity, large inner space, the enhanced spatial density of active site as well as an unimpeded electron transport channel.

Carbon dots (CDs) have both remarkable light-harvesting and electron-transfer/reservoir abilities, which may act as an important component of the microreactor.<sup>18–24</sup> With CDs in a microreactor system, the transportation of photogenerated

<sup>a</sup>Jiangsu Key Laboratory of Advanced Catalytic Materials and Technology, School of Petrochemical Engineering, Changzhou University, Changzhou 213164, China. E-mail: qianliang@cczu.edu.cn; zhongyuli@mail.tsinghua.edu.cn

<sup>b</sup>Institute of Functional Nano and Soft Materials Laboratory (FUNSOM), Jiangsu Key Laboratory for Carbon-Based Functional Materials & Devices, Soochow University, Suzhou 215123, China. E-mail: zhkang@suda.edu.cn

<sup>c</sup>Macao Institute of Materials Science and Engineering, Macau University of Science and Technology, Taipa, 999078, Macau SAR, China. E-mail: zhkang@must.edu.mo

<sup>d</sup>Institute of Advanced Materials, Northeast Normal University, Changchun, 130024, China. E-mail: kangzh@nenu.edu.cn

† Electronic supplementary information (ESI) available. See DOI: <https://doi.org/10.1039/d2ta07217c>

electrons in the encapsulation system will become faster and more efficient.<sup>25</sup> CDs as electron storage containers may capture more electrons from the semiconductor catalyst and regulate the local charge distribution, thus acquiring more electrons to produce  $\text{CH}_4$ .<sup>26</sup> Also, CDs may facilitate the water oxidation reaction to provide more protons for  $\text{CH}_4$  instead of  $\text{H}_2$ .<sup>27</sup> It is predictable that rationally designing and assembling of the CD-modified  $\text{ZnIn}_2\text{S}_4$  microreactor should be a promising approach to achieve the high activity and selectivity of  $\text{CO}_2$ -to- $\text{CH}_4$  conversion. While it is still a big challenge to assemble a productive heterogeneous microreactor by combining active components together through an effective and facile fabrication.

Herein, a carbon dot (CD)-modified  $\text{ZnIn}_2\text{S}_4/\text{TiO}_2$  (CDs/ZIS/ $\text{TiO}_2$ ) microreactor with hollow nanocages and a multi-shell structure was obtained by an ingenious one-step reaction strategy, in which the formed  $\text{TiO}_2$  microcapsule benefited from the corrosion of  $\text{NH}_2\text{-MIL-125}$  caused by thioacetamide (TAA). The as-prepared CDs/ZIS/ $\text{TiO}_2$  microreactors exhibit excellent  $\text{CO}_2$  photoreduction with  $\text{CH}_4$  yield ( $14.9 \mu\text{mol g}^{-1} \text{h}^{-1}$ ) without a sacrificial agent, which is much higher than that of pure  $\text{ZnIn}_2\text{S}_4$ . Besides, the CDs/ZIS/ $\text{TiO}_2$  microreactor presents a highly stable photocatalytic activity after six successive runs. The well-defined architecture with multi-shell structure, high surface area, and large inner space can improve the light absorption ability, shorten the diffusion pathway, and facilitate charge transfer. Importantly, CDs as electron “reservoirs” can effectively capture electrons and inhibit charge recombination. The proposed photocatalytic mechanism and charge transfer process were studied in detail using transient photo-induced voltage (TPV), *in situ* Fourier transform infrared and electron spin resonance (ESR) spectra.

## 2. Experimental section

### 2.1 Synthesis

**2.1.1 Synthesis of  $\text{ZnIn}_2\text{S}_4/\text{TiO}_2$  microcapsules.** A certain amount of the as-prepared  $\text{NH}_2\text{-MIL-125}(\text{Ti})$ <sup>28</sup> was dispersed into the deionized water (50 mL) under ultrasonication for 30 min to obtain a light-yellow solution. Then,  $\text{ZnCl}_2$  (32.2 mg),  $\text{InCl}_3 \cdot 4\text{H}_2\text{O}$  (138.5 mg), and TAA (71 mg) were added to the above mixture and stirred for 1 h at room temperature. Then, the mixture was transferred to an oil bath and kept at  $110^\circ\text{C}$  for 1 h. Finally, the solid product was collected by centrifugation and washed with water and ethanol several times. Finally, the solid product was dried at  $60^\circ\text{C}$  overnight. The resulting  $\text{ZnIn}_2\text{S}_4/\text{TiO}_2$  products with different amounts of  $\text{ZnIn}_2\text{S}_4$  were denoted as  $\text{ZIS}(x)/\text{TiO}_2$ , where  $x$  represents the mass percentage of  $\text{ZnIn}_2\text{S}_4$  in the composite ( $x = 50, 60$ , and  $80 \text{ wt}\%$ ).

**2.1.2 Synthesis of CDs/ $\text{ZnIn}_2\text{S}_4/\text{TiO}_2$  microreactor.** The as-prepared CDs were added to a mixture solution including  $\text{NH}_2\text{-MIL-125}(\text{Ti})$ ,  $\text{ZnCl}_2$ ,  $\text{InCl}_3 \cdot 4\text{H}_2\text{O}$ , TAA, and deionized water, following the same procedure as that of  $\text{ZnIn}_2\text{S}_4/\text{TiO}_2$  microcapsules. The suspension was transferred to an oil bath and kept at  $110^\circ\text{C}$  for 1 h. Finally, the solid product was collected by centrifugation and washed with water and ethanol several times. The optimal weight ratio of  $\text{ZnIn}_2\text{S}_4/\text{TiO}_2$  was selected to

assemble the microreactor, where  $\text{ZIS}(60)/\text{TiO}_2$  was used in the microreactor. The series of CDs/ $\text{ZnIn}_2\text{S}_4(60)/\text{TiO}_2$  ( $y$ -CDs/ZIS/ $\text{TiO}_2$ ) microreactors prepared were denoted as 3-CDs/ZIS/ $\text{TiO}_2$ , 5-CDs/ZIS/ $\text{TiO}_2$ , 10-CDs/ZIS/ $\text{TiO}_2$ , respectively, where  $y$  represented the mass percentage of CDs in the microreactors ( $y = 3, 5$  and  $10 \text{ wt}\%$ ).

## 3. Results and discussion

### 3.1 Material characterization

The synthetic procedure of the CDs/ZIS/ $\text{TiO}_2$  microreactor is schematically presented in Fig. 1a, in which this microreactor was prepared by a one-step *in situ* self-assembly method. The morphological characteristics of the ZIS/ $\text{TiO}_2$  microcapsule and CDs/ZIS/ $\text{TiO}_2$  microreactor were observed from SEM and TEM images. SEM images demonstrated that the pristine  $\text{ZnIn}_2\text{S}_4$  presents flower-like microspheres including numerous nanosheets (Fig. S3a†), while  $\text{NH}_2\text{-MIL-125}$  has a uniform pill-like morphology with an average length of 600 nm (Fig. S3b†). When ZIS/ $\text{TiO}_2$  microcapsule was formed, its morphology was quite different from that of  $\text{NH}_2\text{-MIL-125}$  and  $\text{ZnIn}_2\text{S}_4$  (Fig. S3c†). The microcapsule seems to be the expansion of  $\text{NH}_2\text{-MIL-125}$  caused by the effect of TAA and presents a round spindle shape. Besides, a few nanosheets on the surface belonged to the  $\text{ZnIn}_2\text{S}_4$  layer. Few defects on the surface of the microcapsule can be seen from the SEM and TEM images of ZIS/ $\text{TiO}_2$ , shown in Fig. S3f,† the hollow cavity can be clearly observed, in which the inner space can be found through the

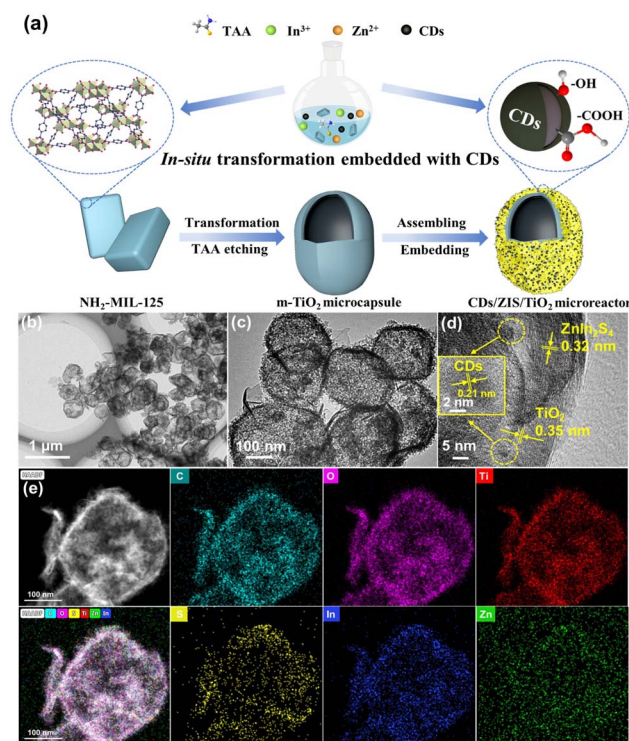


Fig. 1 (a) Schematic illustration for the preparation of CDs/ZIS/ $\text{TiO}_2$  microreactor. (b and c) TEM images, (d) HRTEM image, and (e) EDS mapping of 5-CDs/ZIS/ $\text{TiO}_2$ .

sharp contrast between the rough shell and central void space. Furthermore, due to the growth of the  $\text{ZnIn}_2\text{S}_4$  nanosheet on the  $\text{TiO}_2$  microcapsule, the “double-shell”-like structure can be observed, and the average length of  $\text{ZIS}/\text{TiO}_2$  seems slightly greater than  $\text{NH}_2\text{-MIL-125}$ , demonstrating that TAA affects not only the phase but also the shape of  $\text{NH}_2\text{-MIL-125}$  during the self-assembly process, thus the coexistence of  $\text{ZnIn}_2\text{S}_4$  and  $\text{TiO}_2$  in the microcapsule shell. In order to further confirm the formation of  $\text{TiO}_2$  microcapsule, we investigated the morphology of  $\text{m-TiO}_2$ , where only TAA was added to affect the morphology of  $\text{NH}_2\text{-MIL-125}$ , without the Zn/In ions. From the SEM image, as displayed in Fig. S3g,<sup>†</sup> the as-prepared  $\text{m-TiO}_2$  still exhibits the microcapsule structure, and the HRTEM image of  $\text{m-TiO}_2$  showed the interplanar distance of 0.35 nm (Fig. S3h<sup>†</sup>), due to the (101) crystal plane of anatase  $\text{TiO}_2$ , in agreement with the XRD results. The EDS pattern and elemental mapping (Fig. S3i and S4<sup>†</sup>) of  $\text{m-TiO}_2$  showed that the elements of Ti and O existed without other impurities.

From Fig. 1b, it can be seen that the  $\text{CDs}/\text{ZIS}/\text{TiO}_2$  microreactor maintained its microcapsule structure and the morphology of  $\text{CDs}/\text{ZIS}/\text{TiO}_2$  is similar to that of  $\text{ZIS}/\text{TiO}_2$ , indicating that the microreactor was intact, indicating that CDs coupled with the  $\text{ZIS}/\text{TiO}_2$  microcapsule fabricated a multi-phase microreactor instead of destroying the original shape. From EDS patterns (Fig. S5<sup>†</sup>), Zn, In, S, Ti, O, and C elements can be observed in this microreactor. As shown in Fig. S2,<sup>†</sup> the pristine CDs exhibit well-dispersion with an average diameter of 3 nm, and after the addition of CDs in the *in situ* synthesis, the morphology of  $\text{CDs}/\text{ZIS}/\text{TiO}_2$  was evaluated from the HRTEM image (Fig. 1d). The HRTEM image of  $\text{CDs}/\text{ZIS}/\text{TiO}_2$  exhibits lattice fringes of 0.21, 0.32 and 0.35 nm that are ascribed to the (100), (102) and (101) crystal facets of CDs,  $\text{ZnIn}_2\text{S}_4$  and  $\text{TiO}_2$ ,

respectively, revealing the successful formation of the  $\text{CDs}/\text{ZIS}/\text{TiO}_2$  microreactor.<sup>29–31</sup> From the EDX mapping analysis of  $\text{CDs}/\text{ZIS}/\text{TiO}_2$  (Fig. 1e), the uniform distribution of C, Zn, In, S, Ti, and O elements throughout the microreactor without agglomeration, further confirmed the formation of hierarchical structure.

The crystal structure information of the  $\text{ZIS}/\text{TiO}_2$  microcapsule and  $\text{CDs}/\text{ZIS}/\text{TiO}_2$  microreactor was investigated by XRD. As displayed in Fig. S6,<sup>†</sup> when only TAA reacted with  $\text{NH}_2\text{-MIL-125}$  without Zn and In source, the XRD patterns of  $\text{NH-MIL-125}$  indicated the obvious phase change with the increasing TAA content. When TAA concentration was less than 25%, both the characteristic peaks of  $\text{TiO}_2$  and  $\text{NH}_2\text{-MIL-125}$  were observed, indicating the coexistence of  $\text{TiO}_2$  and  $\text{NH}_2\text{-MIL-125}$ . When the TAA concentration was more than 35%, only the peaks of  $\text{TiO}_2$  at  $25.2^\circ$ ,  $37.9^\circ$ ,  $48.0^\circ$ , and  $62.6^\circ$  belonging to the (101), (004), (200) and (204) lattice planes of anatase phase (JCPDS 21-1272),<sup>32</sup> and the peaks at  $54.3^\circ$  and  $69.1^\circ$  ascribed to (221) and (301) lattice planes of the rutile phase (JCPDS 21-1276),<sup>33</sup> respectively, were observed, indicating that  $\text{NH-MIL-125}$  was completely decomposed to form  $\text{TiO}_2$  in this case. When the Zn and In sources were added,  $\text{ZnIn}_2\text{S}_4$  was formed on the  $\text{TiO}_2$  microcapsule. It can be seen from Fig. 2a and S7<sup>†</sup> that the main peaks of the composite belonged to the characteristic peaks of  $\text{ZnIn}_2\text{S}_4$  at the (006), (102), (110), (116), and (022) lattice planes, and (101) lattice planes of anatase  $\text{TiO}_2$  were observed clearly, indicating the successful synthesis of  $\text{ZIS}/\text{TiO}_2$  microcapsules. The broad peaks of pristine CDs emerge at  $23^\circ$ , corresponding to the (002) crystal plane of graphite, which illustrates the amorphous phase (Fig. S1a<sup>†</sup>).<sup>34</sup> As expected,  $\text{CDs}/\text{ZIS}/\text{TiO}_2$  exhibited similar diffraction peaks to  $\text{ZIS}/\text{TiO}_2$ , and no characteristic peaks indexed to CDs were observed, probably caused by

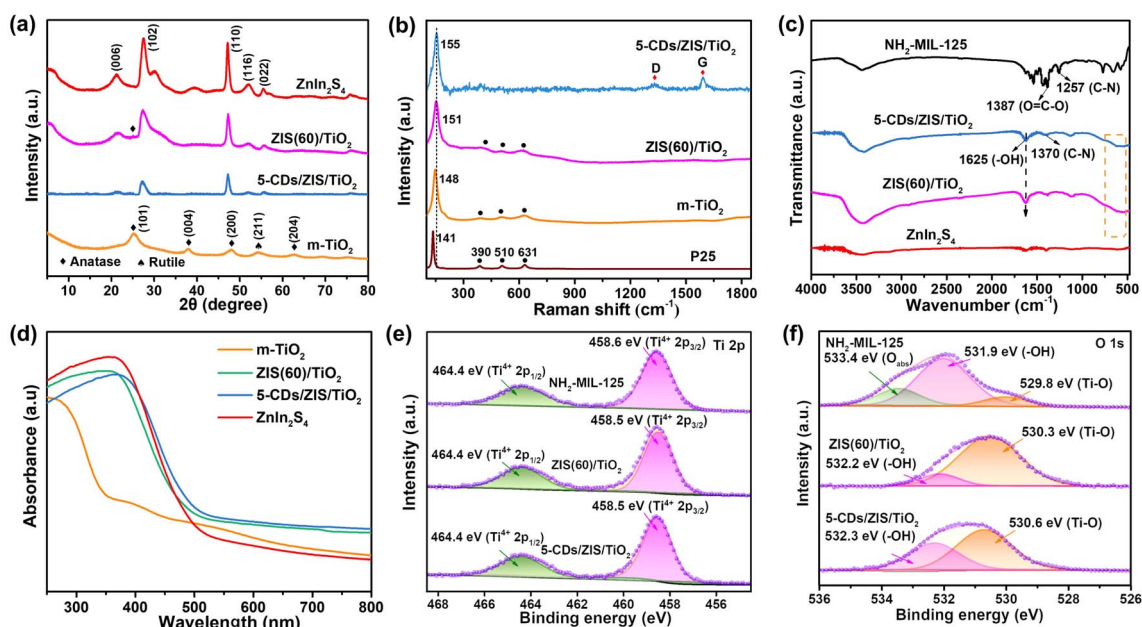


Fig. 2 (a) XRD patterns of  $\text{ZnIn}_2\text{S}_4$ ,  $\text{m-TiO}_2$ ,  $\text{ZIS}(60)/\text{TiO}_2$ , and  $5\text{-CDs}/\text{ZIS}/\text{TiO}_2$ . (b) Raman spectra of P25,  $\text{m-TiO}_2$ ,  $\text{ZIS}(60)/\text{TiO}_2$ , and  $5\text{-CDs}/\text{ZIS}/\text{TiO}_2$ . (c) FT-IR spectra of  $\text{NH}_2\text{-MIL-125}$ ,  $\text{ZnIn}_2\text{S}_4$ ,  $\text{ZIS}(60)/\text{TiO}_2$  and  $5\text{-CDs}/\text{ZIS}/\text{TiO}_2$ . (d) UV-vis spectra of  $\text{ZnIn}_2\text{S}_4$ ,  $\text{m-TiO}_2$ ,  $\text{ZIS}(60)/\text{TiO}_2$ , and  $5\text{-CDs}/\text{ZIS}/\text{TiO}_2$ . High-resolution XPS spectra of (e) Ti 2p and (f) O 1s over  $\text{NH}_2\text{-MIL-125}$ ,  $\text{ZIS}(60)/\text{TiO}_2$ , and  $5\text{-CDs}/\text{ZIS}/\text{TiO}_2$ .

their low content, uniform distribution as well as small particle size, demonstrating that the microreactors were intact after the introduction of CDs through one-step self-assembly method.

To further investigate the structure of the CDs/ZIS/TiO<sub>2</sub> microreactor, Raman spectra were collected and are displayed in Fig. 2b. Since ZnIn<sub>2</sub>S<sub>4</sub> presents a weak Raman signal, we tested the Raman spectrum of m-TiO<sub>2</sub>, in which the peaks of m-TiO<sub>2</sub> at 148, 394, 510, and 631 cm<sup>-1</sup> are ascribed to the E<sub>g</sub>, B<sub>1g</sub>, A<sub>1g</sub>, and E<sub>g</sub> modes, respectively, confirming the successful synthesis of anatase TiO<sub>2</sub>.<sup>35</sup> Compared with commercial P25, the obvious shift of m-TiO<sub>2</sub> at 148 cm<sup>-1</sup> is due to the formation of the microcapsule and the size effect of TiO<sub>2</sub>. For ZIS/TiO<sub>2</sub> and CDs/ZIS/TiO<sub>2</sub>, the further shift at 151 and 155 cm<sup>-1</sup> show that the introduction of ZnIn<sub>2</sub>S<sub>4</sub> and CDs can enhance the interaction of the composite catalyst.<sup>36</sup> Besides, two signals at 1335 and 1594 cm<sup>-1</sup> resulting from the D and G bands of CDs, respectively, were observed, indicating that CDs are embedded in the ZIS/TiO<sub>2</sub>.<sup>37</sup> The FTIR spectra of the ZIS/TiO<sub>2</sub> microcapsule and the CDs/ZIS/TiO<sub>2</sub> microreactor are displayed in Fig. 2c and S8,† respectively, and the functional groups of the as-prepared samples around 3480 cm<sup>-1</sup> belonged to -OH bending vibration.<sup>38</sup> The pristine NH<sub>2</sub>-MIL-125 exhibited the characteristic peaks around 500–800 cm<sup>-1</sup> corresponding to the bending vibrations of the Ti–O–Ti group, the band at 1257 cm<sup>-1</sup> is ascribed to the C–N group, and the bands in the range of 1350–1600 cm<sup>-1</sup> could represent the -COOH group.<sup>39</sup> Although bare ZnIn<sub>2</sub>S<sub>4</sub> has no obvious characteristic peaks, after the formation of ZIS/TiO<sub>2</sub> and CDs/ZIS/TiO<sub>2</sub>, the peaks in the range of 500–700 cm<sup>-1</sup> and the band at 1625 cm<sup>-1</sup> can be clearly observed, which represent the Ti–O group and -OH group, respectively, indicating that NH<sub>2</sub>-MIL-125 was indeed converted to TiO<sub>2</sub> in the microreactor. Due to the small number of CDs, the characteristic peaks belonging to CDs were not observed in the microreactor. The above results verified the coexistence of the anatase TiO<sub>2</sub> phase and CDs in the microreactor.

The UV-vis DRS spectra of CDs/ZIS/TiO<sub>2</sub> microreactors were collected to investigate their optical absorption ability and are shown in Fig. 2d. It was found that NH<sub>2</sub>-MIL-125 exhibited good visible-light absorption, attributable to the absorption of NH<sub>2</sub>-ligand, while the pristine ZnIn<sub>2</sub>S<sub>4</sub> presents an absorption edge around 520 nm. For m-TiO<sub>2</sub>, the absorption edge was increased compared with P25, probably due to the change in morphology, as shown in Fig. S9.† When the ZIS/TiO<sub>2</sub> microcapsule was formed, the absorption edge was slightly decreased in comparison with bare ZnIn<sub>2</sub>S<sub>4</sub>, probably due to the weak light absorption of TiO<sub>2</sub>. After the fabrication of CDs/ZIS/TiO<sub>2</sub>, the extended absorption edges in the visible-light range can be clearly observed, indicative of the strong absorption of CDs. Since the optical bandgap (E<sub>g</sub>) of the photocatalyst is crucial to the determination of the photocatalytic mechanism, E<sub>g</sub> values can be obtained from a Tauc plot on the basis of UV-vis DRS spectra (Fig. S10†). E<sub>g</sub> values of NH<sub>2</sub>-MIL-125, ZnIn<sub>2</sub>S<sub>4</sub>, and m-TiO<sub>2</sub> were calculated to be 2.48, 2.37, and 2.94 eV, respectively.

The specific surface area of the CDs/ZIS/TiO<sub>2</sub> microreactor was obtained from N<sub>2</sub> adsorption-desorption isotherms (Fig. S11†). The pristine NH<sub>2</sub>-MIL-125 exhibited a high BET surface area (1006 m<sup>2</sup> g<sup>-1</sup>) and its N<sub>2</sub> sorption isotherm

belonged to type I, indicating the characteristics of the microporous material.<sup>40</sup> In comparison, pure ZnIn<sub>2</sub>S<sub>4</sub> exhibited a type-IV isotherm with an obvious hysteresis loop, and a BET surface area of 138 m<sup>2</sup> g<sup>-1</sup>. After the formation of the microcapsule, some microporous structure emerges due to the TiO<sub>2</sub> derived from NH<sub>2</sub>-MIL-125, and therefore, the BET surface area of ZIS(60)/TiO<sub>2</sub> was up to 272 m<sup>2</sup> g<sup>-1</sup>, much higher than that of ZnIn<sub>2</sub>S<sub>4</sub>. When CDs were added and the microreactor was constructed, the CDs/ZIS/TiO<sub>2</sub> presented the BET surface area of 206 m<sup>2</sup> g<sup>-1</sup>, slightly lower than that of ZIS/TiO<sub>2</sub>, demonstrating that CDs exist in the microreactor and occupy part of the channel. From the corresponding BJH diagrams (inset), the microcapsule and microreactor exhibit similar pore size distribution, and possessed the coexistence of micropore and mesopore with pore diameters of <20 nm.<sup>41</sup> The rich porosity is conducive to offering more active sites and reducing the mass transfer resistance, which contributes to robust CO<sub>2</sub> photoreduction.

The elemental composition and electron structure of the CDs/ZIS/TiO<sub>2</sub> microreactor were analyzed by XPS spectra. From the XPS survey spectra (Fig. S12a†), the ZIS/TiO<sub>2</sub> microcapsule and CDs/ZIS/TiO<sub>2</sub> microreactor exhibited the expected presence of Ti, O, C, Zn, In, and S, and the peak intensity of the C element in CDs/ZIS/TiO<sub>2</sub> was stronger than that in ZIS/TiO<sub>2</sub>, indicating that CDs were successfully embedded in ZIS/TiO<sub>2</sub>. Besides, the N element was observed in NH<sub>2</sub>-MIL-125 instead of ZIS/TiO<sub>2</sub>, suggesting that the N element was lost during the self-assembly process. As displayed in Fig. 2e, the Ti 2p peaks with binding energies of 458.6 and 464.4 eV were assigned to Ti 2p<sub>3/2</sub> and Ti 2p<sub>1/2</sub>, respectively, indicative of the presence of Ti<sup>4+</sup> in the pristine NH<sub>2</sub>-MIL-125, corresponding to the previous work.<sup>42</sup> For ZIS/TiO<sub>2</sub> and CDs/ZIS/TiO<sub>2</sub>, the peak slightly shifted to the lower binding energy of Ti 2p<sub>3/2</sub>, probably due to the phase change from the Ti–O cluster to TiO<sub>2</sub>.<sup>43</sup> Notably, O 1s peak is of significance for investigating the surface unsaturated surrounding in Ti and further confirmed the formation of metal oxides (Fig. 2f). In the deconvoluted O 1s spectrum of NH<sub>2</sub>-MIL-125, the three signals at 529.8, 531.9, and 533.4 eV correspond to the Ti–O bond, -OH bond and adsorbed oxygen (O<sub>abs</sub>), respectively.<sup>44</sup> However, for ZIS/TiO<sub>2</sub> and CDs/ZIS/TiO<sub>2</sub>, the area of the Ti–O band was significantly enhanced, demonstrating that a large amount of metal oxide was constructed.<sup>45</sup> In addition, the C 1s spectra of NH<sub>2</sub>-MIL-125 presented four deconvoluted signals at 284.8, 285.3, 286.5, and 288.7 eV, which represent the C=C, C–N, C–NH<sub>2</sub>, and C=O bonds, respectively, indicative of the presence of the C–N group (Fig. S12b†).<sup>46</sup> For ZIS/TiO<sub>2</sub> and CDs/ZIS/TiO<sub>2</sub>, the peaks of the amino group disappeared, and more C–C and C=O groups emerged, indicating the presence of surface functional groups such as hydroxyl and carboxyl around catalysts.<sup>47</sup> From the high-resolution spectrum of N 1s (Fig. S12c†), the difference between NH<sub>2</sub>-MIL-125 and ZIS/TiO<sub>2</sub> can be seen clearly. The N 1s spectrum of NH<sub>2</sub>-MIL-125 was deconvoluted into two signals at 399.2 and 402.6 eV, which belong to the amino group (C–N) and imine group (–NH–), respectively,<sup>48</sup> while there were no observable N 1s signals in ZIS/TiO<sub>2</sub> and CDs/ZIS/TiO<sub>2</sub>, suggesting that MOF-topological structure was completely converted into TiO<sub>2</sub>, successfully.

Besides, as for Zn (Fig. S12d†), the binding energies of 1022.3 and 1045.4 eV correspond to Zn 2p<sub>3/2</sub> and Zn 2p<sub>1/2</sub>, respectively, which is typical of Zn<sup>2+</sup> in ZIS/TiO<sub>2</sub> and CDs/ZIS/TiO<sub>2</sub>.<sup>49</sup> For In 3d XPS spectra (Fig. S12e†), the peaks of ZIS/TiO<sub>2</sub> centered at 445.3 and 452.8 eV are due to the In 3d<sub>5/2</sub> and In 3d<sub>3/2</sub>, respectively.<sup>49</sup> Compared with ZIS/TiO<sub>2</sub>, the binding energies of CDs/ZIS/TiO<sub>2</sub> for In 3d region exhibited a slight positive shift, which resulted from the changed electron density caused by the effect of CDs. In Fig. S12f,† the binding energies of S 2p in ZIS/TiO<sub>2</sub> at 162.0 and 163.3 eV are indicative of the presence of S<sup>2-</sup>, and also CDs/ZIS/TiO<sub>2</sub> exhibited a larger positive shift compared with In 3d orbit, suggesting the effective electron transfer.<sup>50</sup>

### 3.2 Photocatalytic CO<sub>2</sub> reduction

With the CDs/ZIS/TiO<sub>2</sub> microreactor as a photocatalyst, the photocatalytic performances for CO<sub>2</sub> reduction were conducted in H<sub>2</sub>O/EA solution without any photosensitizer or sacrificial agent, in which EA could enhance the solubility of CO<sub>2</sub> gas. During these experiments, CO and CH<sub>4</sub> were detected as main products in the as-prepared catalysts under simulated solar light irradiation, as displayed in Fig. 3. Only a small amount of CO product (0.7 μmol g<sup>-1</sup> h<sup>-1</sup>) over pristine NH<sub>2</sub>-MIL-125 was detected, while the bare ZnIn<sub>2</sub>S<sub>4</sub> presented low CO (3.1 μmol g<sup>-1</sup> h<sup>-1</sup>) and CH<sub>4</sub> (0.3 μmol g<sup>-1</sup> h<sup>-1</sup>) yields. After the formation of the ZIS/TiO<sub>2</sub> microcapsule, CO<sub>2</sub> photoreduction was remarkably enhanced compared with the precursors. The different weight ratios of ZnIn<sub>2</sub>S<sub>4</sub> and TiO<sub>2</sub> were considered (Fig. 3b), and the optimal ZIS(60)/TiO<sub>2</sub> exhibited CO and CH<sub>4</sub> yields of up to 12.9 and 7.4 μmol g<sup>-1</sup> h<sup>-1</sup>, respectively. Notably, the introduction of CDs on ZIS(60)/TiO<sub>2</sub> further boosted the photocatalytic

performances, 5-CDs/ZIS/TiO<sub>2</sub> showed the maximum CO (19.2 μmol g<sup>-1</sup> h<sup>-1</sup>) and CH<sub>4</sub> (14.9 μmol g<sup>-1</sup> h<sup>-1</sup>) yields, in which, the concentration of products revealed a linearly enhancing trend with duration time. Such outstanding activity originated from the CDs/ZIS/TiO<sub>2</sub> as a productive heterogeneous microreactor. The yield of CH<sub>4</sub> generation over the as-prepared CDs/ZIS/TiO<sub>2</sub> is regarded as one of the most competitive performances for ZnIn<sub>2</sub>S<sub>4</sub>-based catalysts after an extensive literature search in the field of similar photocatalysts as illustrated in Table S5.†

Based on electron consumption rates ( $R_{\text{electron}}$ , CH<sub>4</sub>: 8e<sup>-</sup>; CO: 2e<sup>-</sup>), CH<sub>4</sub> selectivity was evaluated by the following equation: CH<sub>4</sub> selectivity (%) =  $[8R(\text{CH}_4)]/[2R(\text{CO}) + 8R(\text{CH}_4)] \times 100\%$ , where  $R(\text{CO})$  and  $R(\text{CH}_4)$  are the conversion rates of CO and CH<sub>4</sub>, respectively. As displayed in Fig. 3d and S14,† the 5-CDs/ZIS/TiO<sub>2</sub> microreactor exhibited the highest CH<sub>4</sub> selectivity (75.6%), and  $R_{\text{electron}}$  was up to 157.6 μmol g<sup>-1</sup> h<sup>-1</sup>, which were 1.9 and 18.3 times higher those of ZIS(60)/TiO<sub>2</sub> and bare ZnIn<sub>2</sub>S<sub>4</sub>, respectively, indicating that e more protons formed in the microreactor can facilitate the CH<sub>4</sub> production from CO<sub>2</sub> reduction. Importantly, O<sub>2</sub> as the main oxidation product was observed, as displayed in Fig. S16,† verifying the overall photocatalytic CO<sub>2</sub> reduction. The O<sub>2</sub> yield of 5-CDs/ZIS/TiO<sub>2</sub> (11.3 μmol h<sup>-1</sup> g<sup>-1</sup>) was higher than that of ZIS(60)/TiO<sub>2</sub> (7.1 μmol h<sup>-1</sup> g<sup>-1</sup>), indicating that CDs have a positive effect on H<sub>2</sub>O oxidation reaction. Additionally, the stoichiometric ratio of the consumed electrons and holes for ZIS(60)/TiO<sub>2</sub> and 5-CDs/ZIS/TiO<sub>2</sub> was 1.1 and 1.2, respectively, which illustrated that the two values are close to 1. To further evaluate the oxidation capacity of the CDs/ZIS/TiO<sub>2</sub> microreactor, oxygen evolution reaction (OER) was revealed by the linear sweep voltammetry (LSV) performances (Fig. S17†). The increased current density of

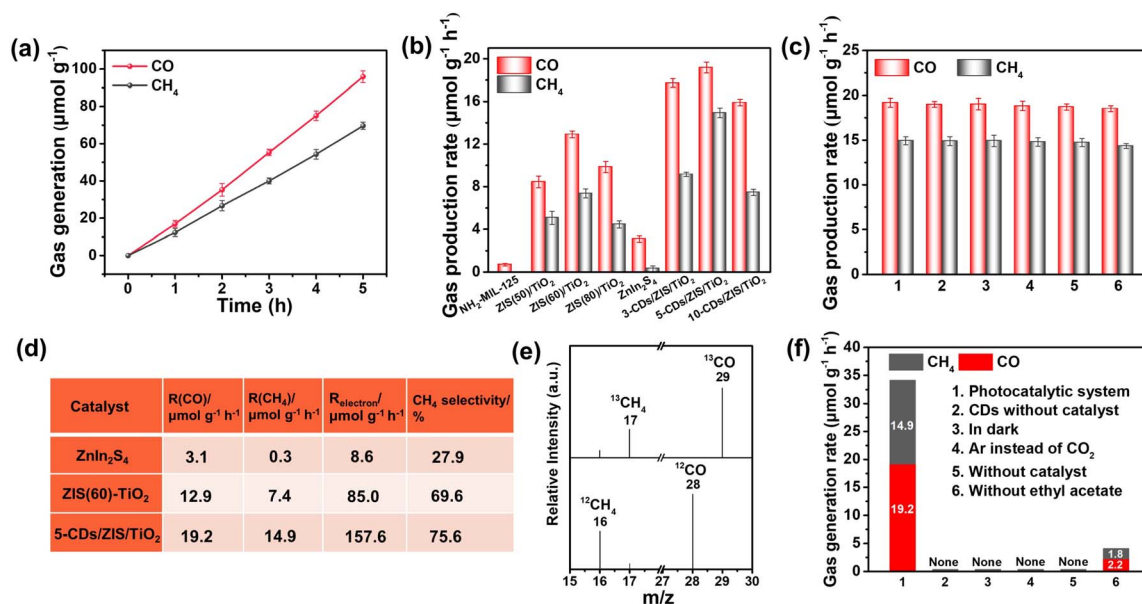


Fig. 3 (a) Time–yield plots of 5-CDs/ZIS/TiO<sub>2</sub> under AM 1.5 G simulated solar irradiation. (b) Photocatalytic CO<sub>2</sub> reduction performances of different catalysts. (c) Photocatalytic cycling stability of 5-CDs/ZIS/TiO<sub>2</sub>. (d) Summary of the photocatalytic performances of ZnIn<sub>2</sub>S<sub>4</sub>, ZIS(60)/TiO<sub>2</sub>, and 5-CDs/ZIS/TiO<sub>2</sub>. (e) GC-MS analysis of CO generated from the <sup>13</sup>CO<sub>2</sub> isotope experiment. (f) Production rates of CO and CH<sub>4</sub> over 5-CDs/ZIS/TiO<sub>2</sub> under various reaction conditions.

ZIS(60)/TiO<sub>2</sub> was observed compared with the pristine ZnIn<sub>2</sub>S<sub>4</sub>, indicating that the microcapsule presented an excellent OER activity. Obviously, after the formation of the CDs-modified microreactor, all the CDs/ZIS/TiO<sub>2</sub> samples possessed further enhanced current density, meaning that the microreactor with higher OER performance drove the complete CO<sub>2</sub> reduction reaction.

The long-term durability of CDs/ZIS/TiO<sub>2</sub> was investigated by cycle tests as displayed in Fig. 3c. After six successive cycles over 30 h, a negligible decrease in the photocatalytic performance of 5-CDs/ZIS/TiO<sub>2</sub> was detected, with only *ca.* 3.6% and 4.0% deactivation of CO and CH<sub>4</sub> yields, respectively. The <sup>13</sup>C labeled isotope experiments confirmed that the generated CO and CH<sub>4</sub> indeed originated from catalysts instead of other carbon sources, as illustrated in Fig. 3e. <sup>13</sup>CO (*m/z* = 29) and <sup>13</sup>CH<sub>4</sub> (*m/z* = 17) were observed, revealing that the products are from the CO<sub>2</sub> photoreduction. Furthermore, the controlled tests were performed to determine the origin of the products (Fig. 3f). Negligible amounts of carbon-containing products were observed when the reaction system was tested without the photocatalyst, absence of light irradiation, and in Ar atmosphere instead of high-purity CO<sub>2</sub>, demonstrating that the photo-excited process was indispensable for this reaction, and the other carbon impurities existed in the photocatalyst and the reaction system could not afford any CO<sub>2</sub> reduction products.

### 3.3 Mechanism for the CO<sub>2</sub> photoreduction

Steady-state and time-resolved PL spectra were used as powerful tools to investigate the electron transfer of the CDs/ZIS/TiO<sub>2</sub> microreactor. As displayed in Fig. 4a, the PL intensity of ZIS/TiO<sub>2</sub> decreased in comparison with the pure ZnIn<sub>2</sub>S<sub>4</sub>, which indicated that the formed hierarchical hollow morphology with a shorter charge transfer distance could reduce the charge

recombination. After the introduction of CDs, the interfacial interaction between ZnIn<sub>2</sub>S<sub>4</sub> and TiO<sub>2</sub> became stronger, which can remarkably improve the charge transfer efficiency, leading to CDs/ZIS/TiO<sub>2</sub> with the lowest PL intensity.<sup>51</sup> The average PL lifetimes ( $\tau_{\text{ave}}$ ) of the representative catalysts were further investigated using TR-PL spectra with values of 1.62, 1.22, 1.06 ns for ZnIn<sub>2</sub>S<sub>4</sub>, ZIS(60)/TiO<sub>2</sub> and 5-CDs/ZIS/TiO<sub>2</sub>, respectively, as shown in Fig. 4b. The PL lifetime of ZIS(60)/TiO<sub>2</sub> presents a shorter  $\tau_{\text{ave}}$  than ZnIn<sub>2</sub>S<sub>4</sub>, attributable to fast electron transfer on the surface of the microcapsule, resulting from intimate contact. The faster PL decay and shorter  $\tau_{\text{ave}}$  in 5-CDs/ZIS/TiO<sub>2</sub> indicate that CDs indeed act as charge mediators in a microreactor.<sup>52</sup> The observations of decay in both steady-state and time-resolved PL results demonstrate that microcapsule and multi-phase microreactors can effectively suppress the charge carrier recombination.

The electrochemical performances were further studied to analyze the effect of the multi-phase microreactor on the photoinduced charge separation efficiency. The photocurrent of ZIS(60)/TiO<sub>2</sub> was much higher than that of ZnIn<sub>2</sub>S<sub>4</sub> and unconverted NH<sub>2</sub>-MIL-125 under simulated sunlight irradiation (Fig. 4c). Also, 5-CDs/ZIS/TiO<sub>2</sub> indicates that the further enhanced current density, which implies that CDs in the microreactor can accelerate the electron transfer rate.<sup>54</sup>

Corresponding to the photocurrent results, ZIS(60)/TiO<sub>2</sub> and 5-CDs/ZIS/TiO<sub>2</sub> showed smaller radii in the EIS Nyquist diagram (Fig. 4d), which represented the decreasing charge transfer resistance, facilitating the charge transport and boosting reaction kinetics in photocatalytic performance.<sup>53</sup> Furthermore, the flat-band potentials ( $E_{\text{FB}}$ ) of ZnIn<sub>2</sub>S<sub>4</sub> and TiO<sub>2</sub> were obtained from Mott-Schottky (M-S) plots at frequencies of 1000, 1500, and 2000 Hz (Fig. 4e and f).<sup>54</sup> The plots of ZnIn<sub>2</sub>S<sub>4</sub> and TiO<sub>2</sub> display positive slopes, indicative of typical n-type

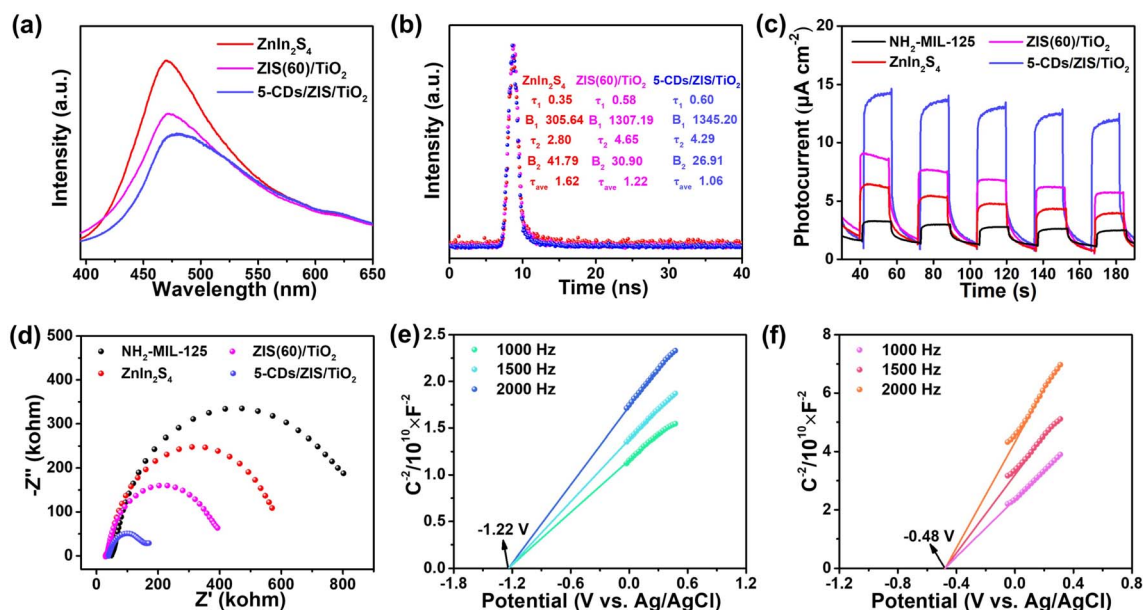


Fig. 4 (a) PL spectra and (b) TRPL spectra of ZnIn<sub>2</sub>S<sub>4</sub>, ZIS(60)/TiO<sub>2</sub>, and 5-CDs/ZIS/TiO<sub>2</sub>. (c) Photocurrent responses and (d) EIS Nyquist plots of NH<sub>2</sub>-MIL-125, ZnIn<sub>2</sub>S<sub>4</sub>, ZIS(60)/TiO<sub>2</sub>, and 5-CDs/ZIS/TiO<sub>2</sub>. Mott-Schottky plots of (e) ZnIn<sub>2</sub>S<sub>4</sub> and (f) m-TiO<sub>2</sub>.

semiconductors. The  $E_{\text{FB}}$  values of  $\text{ZnIn}_2\text{S}_4$  ( $-1.22$  V vs. Ag/AgCl) and  $\text{m-TiO}_2$  ( $-0.48$  V vs. Ag/AgCl) were determined by extrapolating the M-S plots, and correspondingly,  $E_{\text{FB}}$  values are  $-1.02$  and  $-0.28$  V (vs. NHE) for  $\text{ZnIn}_2\text{S}_4$  and  $\text{m-TiO}_2$  according to the  $E_{\text{NHE}} = E_{\text{Ag/AgCl}} + 0.197$ ,<sup>55</sup> respectively, where  $E_{\text{FB}}$  values are close to the conduction band ( $E_{\text{CB}}$ ) potentials of n-type semiconductor.<sup>56</sup> Consequently,  $E_{\text{CB}}$  values of  $\text{ZnIn}_2\text{S}_4$  and  $\text{m-TiO}_2$  are  $-1.02$  and  $-0.28$  V (vs. NHE), respectively, and together with band gaps ( $E_{\text{g}}$ ) from the Tauc plots, the corresponding valence band values ( $E_{\text{VB}}$ ) of  $\text{ZnIn}_2\text{S}_4$  and  $\text{m-TiO}_2$  are  $1.35$  V and  $2.66$  V (vs. NHE), respectively.

Transient photovoltage (TPV) tests were performed to analyze the charge transfer kinetics on the interfaces of the photocatalysts. The TPV relaxation curves of  $\text{m-TiO}_2$ ,  $\text{ZnIn}_2\text{S}_4$ ,  $\text{ZIS}/\text{TiO}_2$ , and  $\text{CDs}/\text{ZIS}/\text{TiO}_2$  are shown in Fig. 5a. Furthermore, as shown in Fig. 5b, the electron recombination rates existing in the photocatalysts were investigated by the use of the attenuation constants ( $\tau$ ). The  $\tau$ s of  $\text{m-TiO}_2$  and  $\text{ZnIn}_2\text{S}_4$  were  $0.682$  and  $0.609$  ms, respectively, while the  $\tau$  of  $\text{ZIS}/\text{TiO}_2$  was  $0.544$  ms. The reason for the smaller  $\tau$  of  $\text{ZIS}/\text{TiO}_2$  is that the formation of the heterojunction between  $\text{m-TiO}_2$  and  $\text{ZnIn}_2\text{S}_4$  causes a part of the charges to recombine before being collected by the working electrode. In addition, the formation of the heterojunction is beneficial for charge transfer. The  $\tau$  of  $\text{CDs}/\text{ZIS}/\text{TiO}_2$  is  $0.421$  ms, revealing that the addition of CDs further facilitates electron transport. As shown in Fig. 5c,  $t_{\text{max}}$  was used to estimate the rate of the charge extraction process. There is a great difference between the  $t_{\text{max}}$  of  $\text{m-TiO}_2$  ( $t_{\text{max}1} = 0.256$  ms) and  $\text{ZnIn}_2\text{S}_4$  ( $t_{\text{max}2} = 0.101$  ms). However, compared with that of  $\text{m-TiO}_2$ ,  $t_{\text{max}3}$  ( $0.114$  ms) becomes much smaller, indicating that the integration of  $\text{m-TiO}_2$  and  $\text{ZnIn}_2\text{S}_4$  promotes the charge extraction process. After the addition of CDs,  $t_{\text{max}4}$  ( $0.133$  ms) is still much

smaller than that of  $\text{m-TiO}_2$ , proving that the addition of CDs also accelerates the charge extraction process. Fig. 5d shows the area of the shadow part (A) of  $\text{m-TiO}_2$ ,  $\text{ZnIn}_2\text{S}_4$ ,  $\text{ZIS}/\text{TiO}_2$ , and  $\text{CDs}/\text{ZIS}/\text{TiO}_2$ , which correspond to the maximum charge extraction of the catalysts. It is worth noting that the A of  $\text{m-TiO}_2$  ( $A_1 = 0.192$ ) and  $\text{ZnIn}_2\text{S}_4$  ( $A_2 = 0.0511$ ) are larger than that of  $\text{ZIS}/\text{TiO}_2$  ( $A_3 = 0.0341$ ), which is attributed to the recombination of the charge on heterojunction interfaces after being excited by the laser, resulting in the smaller amounts of charges collected by the working electrode. Furthermore, the A of  $\text{CDs}/\text{ZIS}/\text{TiO}_2$  ( $A_4 = 0.0934$ ) is larger than that of  $\text{ZIS}/\text{TiO}_2$ , demonstrating that CDs can enhance the electron extraction ability of the photocatalyst. The surface effective charge ( $n_e$ ) is used to further determine the three eigenvalues of TPV ( $\tau$ ,  $t_{\text{max}}$ , A), which can be calculated from the equation of  $n_e = (A \times \tau)/t_{\text{max}}$ . For photocatalysts, the value of  $n_e$  represents the amount of the charge that is involved in the photocatalytic redox reaction.<sup>57</sup> The  $n_e$  of  $\text{m-TiO}_2$ ,  $\text{ZnIn}_2\text{S}_4$ ,  $\text{ZIS}/\text{TiO}_2$ , and  $\text{CDs}/\text{ZIS}/\text{TiO}_2$  are  $0.510$ ,  $0.307$ ,  $0.162$ , and  $0.295$ , respectively. Similarly, the  $n_e$  of  $\text{ZIS}/\text{TiO}_2$  becomes smaller than those of  $\text{m-TiO}_2$  and  $\text{ZnIn}_2\text{S}_4$ , which was also caused by the heterojunction formed between the two components. The  $n_e$  of  $\text{CDs}/\text{ZIS}/\text{TiO}_2$  increases by ca. 1.82 times compared with that of  $\text{ZIS}/\text{TiO}_2$ , suggesting that the introduction of CDs is beneficial for the photocatalytic reaction. In summary, the heterojunction formed between  $\text{m-TiO}_2$  and  $\text{ZnIn}_2\text{S}_4$  facilitated the charge transfer process. In addition, CDs not only play the role of regulating the charge transfer process but also improve the ability of the photocatalyst to extract electrons for the photocatalytic reaction.

*In situ* TPV experiments were performed to understand the photocatalytic reaction over the catalysts. Fig. 6 displays the *in situ* TPV results of  $\text{m-TiO}_2$  and  $\text{ZnIn}_2\text{S}_4$  under an atmosphere of  $\text{N}_2$ -saturated MeCN,  $\text{CO}_2$ -saturated MeCN, and  $0.5$  vol%  $\text{H}_2\text{O}/\text{MeCN}$  (v/v), respectively. Compared with  $\text{m-TiO}_2$ , the TPV intensity of  $\text{ZnIn}_2\text{S}_4$  exhibits a sharper decrease when the

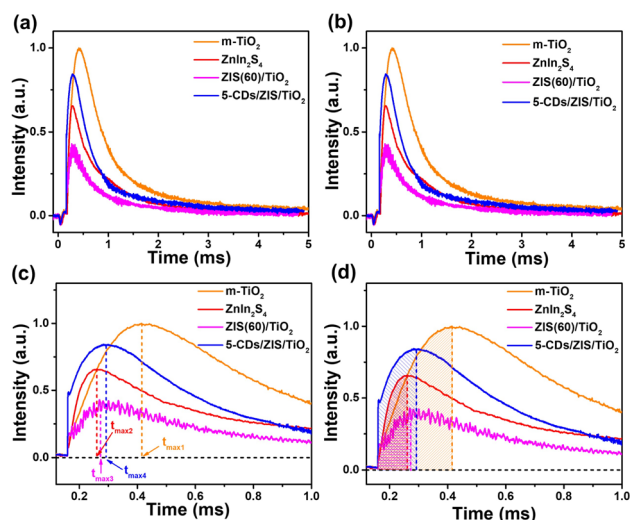


Fig. 5 Comparison of the TPV curves of  $\text{m-TiO}_2$ ,  $\text{ZnIn}_2\text{S}_4$ ,  $\text{ZIS}(60)/\text{TiO}_2$ , and  $5\text{-CDs}/\text{ZIS}/\text{TiO}_2$ . (a) TPV relaxation curves of  $\text{m-TiO}_2$ ,  $\text{ZnIn}_2\text{S}_4$ ,  $\text{ZIS}(60)/\text{TiO}_2$  and  $5\text{-CDs}/\text{ZIS}/\text{TiO}_2$ . (b) The attenuation constants ( $\tau$ ) of the charge recombination process. (c) Charge extraction rate ( $t_{\text{max}}$ ) of  $\text{m-TiO}_2$ ,  $\text{ZnIn}_2\text{S}_4$ ,  $\text{ZIS}(60)/\text{TiO}_2$  and  $5\text{-CDs}/\text{ZIS}/\text{TiO}_2$ . (d) The maximum electron extraction of  $\text{m-TiO}_2$ ,  $\text{ZnIn}_2\text{S}_4$ ,  $\text{ZIS}(60)/\text{TiO}_2$  and  $5\text{-CDs}/\text{ZIS}/\text{TiO}_2$ .

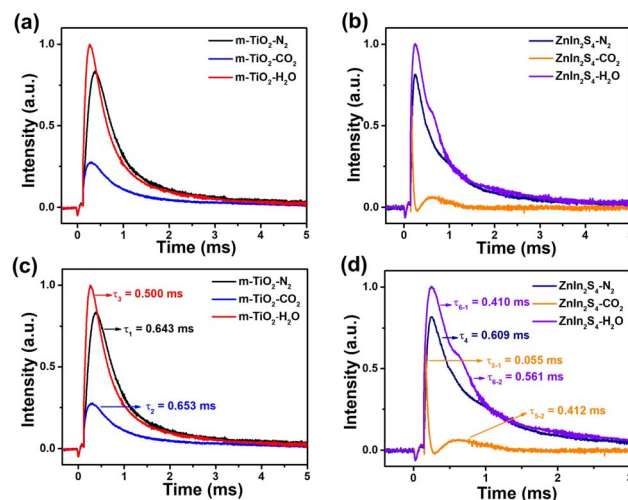


Fig. 6 (a, b) Comparison of the *in situ* TPV curves of  $\text{m-TiO}_2$  and  $\text{ZnIn}_2\text{S}_4$  under  $\text{N}_2$ -saturated MeCN,  $\text{CO}_2$ -saturated MeCN, and  $0.5$  vol%  $\text{H}_2\text{O}/\text{MeCN}$  (v/v). (c, d) The corresponding attenuation constants ( $\tau$ ) of the charge recombination process.

atmosphere changes from  $N_2$ -saturated MeCN to  $CO_2$ -saturated MeCN, indicating that  $ZnIn_2S_4$  provides active sites for the  $CO_2$  reduction reaction, which consumes electrons. Similarly, the  $H_2O$  oxidation reaction consumes holes, which will lead to an increase in TPV intensity. However, the increase of TPV intensity of m- $TiO_2$  and  $ZnIn_2S_4$  are close when the atmosphere changes from  $N_2$ -saturated MeCN to 0.5 vol%  $H_2O$ /MeCN (v/v). Therefore, in order to further analyze the active sites of  $H_2O$  oxidation, the attenuation constants ( $\tau$ ) of the *in situ* TPV curves were calculated, as shown in Fig. 6c and d. It is worth noting that, for  $ZnIn_2S_4$ , there exist two attenuation processes both in  $CO_2$ -saturated and 0.5 vol%  $H_2O$ /MeCN (v/v). Therefore, after calculating the  $\tau$  of each attenuation process ( $\tau_{5-1} = 0.055$  ms,  $\tau_{5-2} = 0.412$  ms,  $\tau_{6-1} = 0.410$  ms,  $\tau_{6-2} = 0.561$  ms), the average  $\tau$ s of  $ZnIn_2S_4$  under  $CO_2$ -saturated and 0.5 vol%  $H_2O$ /MeCN (v/v) ( $\tau_{5avg} = 0.190$  ms,  $\tau_{6avg} = 0.490$  ms) were calculated using the formula (x) provided in the ESI.† The changing percentage of  $\tau$  ( $\Delta\tau$ ) was calculated using the following formula ( $\Delta\tau = (\tau_{N_2} - \tau_{H_2O/CO_2})/\tau_{N_2} \times 100\%$ ) to study the influence of  $CO_2$  or  $H_2O$  on charge recombination process. For m- $TiO_2$ ,  $\Delta\tau(H_2O)$  (22.2%) is much higher than  $\Delta\tau(CO_2)$  (1.56%), which proves that the introduction of  $H_2O$  makes great effect on its charge recombination process, suggesting that m- $TiO_2$  provides active sites for the  $H_2O$  oxidation reaction.<sup>31,34</sup> Similarly, for  $ZnIn_2S_4$ ,  $\Delta\tau(CO_2)$  (68.8%) is much higher than  $\Delta\tau(H_2O)$  (19.5%), indicating that  $ZnIn_2S_4$  provided active sites for the  $CO_2$  reduction reaction.<sup>34,58</sup>

Electron spin resonance (ESR) spectra of CDs/ZIS/ $TiO_2$  were used to further ascertain the photocatalytic mechanism as displayed in Fig. 7a. The obvious DMPO- $\cdot O_2^-$  signals exhibit that the generated electrons on CDs/ZIS/ $TiO_2$  can effectively produce  $\cdot O_2^-$  species, which means that the position of the electrons on the CB is more negative than the potential of superoxide radical ( $O_2/\cdot O_2^-$ ,  $-0.33$  eV).<sup>59</sup> Thus, the above results indicate that the electrons are accumulated on the CB of  $ZnIn_2S_4$  instead of m- $TiO_2$ , which is consistent with the TPV results, both confirming the formation of the Z-scheme mechanism.<sup>60</sup> Besides, we conducted *in situ* FTIR spectroscopy to illustrate the reaction pathway in the  $CO_2$  photoreduction over the CDs/ZIS/ $TiO_2$

microreactor, as displayed in Fig. 7b. It is seen that some peaks of multiple intermediate products emerge, which gradually become stronger with the extension of the irradiation time. After  $CO_2$  and  $H_2O$  gas were adsorbed on CDs/ZIS/ $TiO_2$  in the dark for 30 min, bicarbonate species ( $HCO_3^-$ , 1223, 1398, 1436, 1455 and 1475  $cm^{-1}$ ),<sup>61</sup> monodentate carbonate species (m- $CO_3^{2-}$ , 1418, 1488, 1541 and 1557  $cm^{-1}$ ) and bidentate carbonate species (b- $CO_3^{2-}$ , 1387, 1524 and 1631  $cm^{-1}$ ) were observed in the reaction process,<sup>62,63</sup> revealing that the absorbed  $CO_2$  and dissociative  $H_2O$  molecules exist on the surface of CDs/ZIS/ $TiO_2$ . Besides, new peaks emerge and the active  $CO_2^-$  peaks at 1677  $cm^{-1}$  can be observed. The peaks of formaldehyde ( $HCHO^-$ , 1507 and 1788  $cm^{-1}$ ), methoxy groups ( $CH_3O^-$ , 1688 and 1734  $cm^{-1}$ ), formic acid species ( $HCOO^-$ , 1641 and 1658  $cm^{-1}$ ), and carboxylate species ( $COO^-$ , 1350  $cm^{-1}$ ) are detected, indicating that they are primary intermediates during  $CO_2$  photoreduction.<sup>64–66</sup> Besides, there are no  $CH_4$  peaks, probably due to its nonpolar as well as low affinity.

According to the *in situ* FTIR results,  $HCHO^-$ ,  $CH_3O^-$ ,  $HCOO^-$  and  $COO^-$  groups are the significant intermediates, and coupled with the TPV and ESR results, the formed Z-scheme over CDs/ZIS/ $TiO_2$  was deduced, as shown in Fig. S18.† Under sunlight irradiation, the photoinduced electrons in the CB of m- $TiO_2$  recombine with the holes in the VB of  $ZnIn_2S_4$ , and meanwhile, the accumulation of electrons on the CB of  $ZnIn_2S_4$  and holes on the VB of m- $TiO_2$  possesses strong redox ability for  $CO_2$  reduction and  $O_2$  oxidation.<sup>67</sup> Besides, the CDs in this heterostructure act as an electron conductor and reservoir, in which electrons transported to the surface are captured by CDs, further reducing the charge recombination to promote the redox reaction. As for the formed microreactor, the numerous ultrathin nanosheets as the outer layer are beneficial to CD implantation and  $CO_2$  adsorption. Furthermore, the multi-shell structure, high surface area, and large inner space can promote light utilization by multiple reflections, and facilitate the fast diffusion of gaseous products.

## 4. Conclusions

In summary, we have demonstrated a novel CDs/ $ZnIn_2S_4$ / $TiO_2$  microreactor prepared using a MOF-mediated strategy. During the synthetic process, the thioacetamide (TAA) can facilitate the dissolution of the inner core for  $NH_2$ -MIL-125 to form  $TiO_2$  microcapsules, and with the precipitation of  $Zn^{2+}/In^{3+}$  ions and CDs, a novel productive heterogeneous microreactor with multi-shell structure was obtained. The obtained CDs/ZIS/ $TiO_2$  exhibited high photocatalytic performance and selectivity for  $CO_2$  photoreduction into  $CH_4$  without any sacrificial agent. The yield of  $CH_4$  over optimal CDs/ZIS/ $TiO_2$  was up to 14.9  $\mu mol\ g^{-1}\ h^{-1}$  with  $CH_4$  selectivity of 75.6%, and the  $R_{electron}$  reaches 157.6  $\mu mol\ g^{-1}\ h^{-1}$ . The *in situ* TPV measurements indicated that m- $TiO_2$  provided active sites for the  $H_2O$  oxidation reaction, and  $ZnIn_2S_4$  provided active sites for the  $CO_2$  reduction reaction. Coupled with ESR, photoelectrochemical and *in situ* Fourier transform infrared spectra, a Z-scheme mechanism for CDs/ZIS/ $TiO_2$  is proposed. Furthermore, the CDs in this microreactor as an electron acceptor play a significant role in the improvement

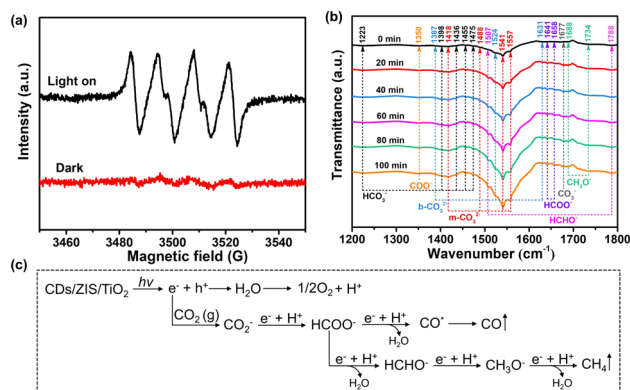


Fig. 7 (a) ESR spectra of DMPO  $\cdot O_2^-$  on 5-CDs/ZIS/ $TiO_2$ . (b) *In situ* DRIFTS spectra of surface adsorbed  $CO_2$  species and photocatalytic  $CO_2$  reduction intermediates on 5-CDs/ZIS/ $TiO_2$ . (c) Photocatalytic reaction pathways over CDs/ZIS/ $TiO_2$ .

of charge separation efficiency. This work not only provides an effective strategy to construct MOF-derived productive heterogeneous microreactor for photocatalytic CO<sub>2</sub> conversion but is also an inspiration for developing the integrated catalytic system in the field of artificial photosynthesis.

## Conflicts of interest

There are no conflicts to declare.

## Acknowledgements

This work is supported by the National Key Basic Research Program of China (2020YFA0406104/2020YFA0406101), the National MCF Energy R&D Program (2018YFE0306105), the Innovative Research Group Project of the National Natural Science Foundation of China (51821002), National Natural Science Foundation of China (51725204, 51972216, 21876015, 52272043, 52271223, 52202107, 52201269), Natural Science Foundation of Jiangsu Province (BK20220028, BK20190041), Natural Science Foundation of Jiangsu Province-Excellent Youth Foundation (BK20190102), Key-Area Research and Development Program of Guangdong Province (2019B010933001), Collaborative Innovation Center of Suzhou Nano Science & Technology, Qinglan Project Foundation of Jiangsu Province, the Priority Academic Program Development of Jiangsu Higher Education Institutions (PAPD), and the 111 Project.

## Notes and references

- 1 S. F. Ji, Y. Qu, T. Wang, Y. J. Chen, G. F. Wang, X. Li, J. C. Dong, Q. Y. Chen, W. Y. Zhang, Z. D. Zhang, S. Y. Liang, R. Yu, Y. Wang, D. S. Wang and Y. D. Li, *Angew. Chem., Int. Ed.*, 2020, **59**, 10651–10657.
- 2 C. L. Wang, Z. X. Sun, Y. Zheng and Y. H. Hu, *J. Mater. Chem. A*, 2019, **7**, 865–887.
- 3 I. Shown, S. Samireddi, Y. C. Chang, R. Putikam, P. Chang, A. Sabbah, F. Fu, W. Chen, C. Wu, T. Yu, P. Chung, M. C. Lin, L. Chen and K. Chen, *Nat. Commun.*, 2018, **9**, 169.
- 4 J. Li, H. L. Huang, W. J. Xue, K. Sun, X. H. Song, C. R. Wu, L. Nie, Y. Li, C. Y. Liu, Y. Pan, H. L. Jiang, D. H. Mei and C. L. Zhong, *Nat. Catal.*, 2021, **4**, 719–729.
- 5 Y. J. Ma, X. X. Yi, S. L. Wang, T. Li, B. Tan, C. C. Chen, T. Majima, E. R. Waclawik, H. Y. Zhu and J. Y. Wang, *Nat. Commun.*, 2022, **13**, 1400.
- 6 H. Wu, X. Y. Kong, X. M. Wen, S. Chai, E. C. Lovell, J. W. Tang and Y. H. Ng, *Angew. Chem., Int. Ed.*, 2021, **60**, 8455–8459.
- 7 S. L. Wang, M. Xu, T. Y. Peng, C. X. Zhang, T. Li, I. Hussain, J. Y. Wang and B. Tan, *Nat. Commun.*, 2019, **10**, 676.
- 8 Y. Zhang, Y. X. Wu, L. Wan, H. J. Ding, H. X. Li, X. Y. Wang and W. H. Zhang, *Appl. Catal., B*, 2022, **311**, 121255.
- 9 S. B. Wang, B. Y. Guan and X. W. Lou, *J. Am. Chem. Soc.*, 2018, **140**, 5037–5040.
- 10 K. Zhu, J. O. Yang, Q. Zeng, S. G. Meng, W. Teng, Y. H. Song, S. Tang and Y. J. Cui, *Chin. J. Catal.*, 2020, **41**, 454–463.
- 11 P. She, B. Y. Guan, J. Y. Sheng, Y. Y. Qi, G. Y. Qiao, H. B. Rui, G. Y. Lu, J. S. Qin and H. Rao, *Catal. Sci. Technol.*, 2022, **12**, 1092–1099.
- 12 S. T. Wu, Z. Xin, S. C. Zhao and S. T. Sun, *Nano Res.*, 2019, **12**, 2736–2742.
- 13 T. He, X. B. Xu, B. Ni, H. F. Lin, C. Z. Li, W. P. Hu and X. Wang, *Angew. Chem., Int. Ed.*, 2018, **57**, 10148–10152.
- 14 Y. Liu, X. F. Zhou, Z. R. Jia, H. J. Wu and G. L. Wu, *Adv. Funct. Mater.*, 2022, **32**, 2204499.
- 15 H. T. Fan, Y. J. Jin, K. C. Liu and W. S. Liu, *Adv. Sci.*, 2022, **9**, 2104579.
- 16 H. J. Xu, C. F. Shan, X. X. Wu, M. Z. Sun, B. Huang, Y. Tang and C. H. Yan, *Energy Environ. Sci.*, 2020, **13**, 2949–2956.
- 17 R. Bibi, H. L. Huang, M. Kalulu, Q. H. Shen, L. F. Wei, O. Oderinde, N. X. Li and J. C. Zhou, *ACS Sustainable Chem. Eng.*, 2019, **7**, 4868–4877.
- 18 Q. Y. Wu, J. J. Cao, X. Wang, Y. Liu, Y. J. Zhao, H. Wang, Y. Liu, H. Huang, F. Liao, M. W. Shao and Z. H. Kang, *Nat. Commun.*, 2021, **12**, 483.
- 19 H. Q. Song, J. K. Yu, Z. Y. Tang, B. Yang and S. Y. Lu, *Adv. Energy Mater.*, 2022, **12**, 2102573.
- 20 J. Wu, Y. D. Han, Y. C. Bai, X. T. Wang, Y. J. Zhou, W. X. Zhu, T. W. He, Y. M. Wang, H. Huang, Y. Liu and Z. H. Kang, *Adv. Funct. Mater.*, 2022, **32**, 2203647.
- 21 Y. J. Dong, Q. Han, Q. Y. Hu, C. J. Xu, C. Z. Dong, Y. Peng, Y. Ding and Y. Q. Lan, *Appl. Catal., B*, 2021, **293**, 120214.
- 22 B. Li, W. Peng, J. Zhang, J. C. Lian, T. Huang, N. Cheng, Z. Y. Luo, W. Q. Huang, W. Y. Hu, A. L. Pan, L. Jiang and G. F. Huang, *Adv. Funct. Mater.*, 2021, **31**, 2100816.
- 23 Y. J. Zhao, L. L. Xu, X. Wang, Z. Z. Wang, Y. Liu, Y. Wang, Q. L. Wang, Z. T. Wang, H. Huang, Y. Liu, W. Y. Wong and Z. H. Kang, *Nano Today*, 2022, **43**, 101428.
- 24 Y. Liu, X. Wang, Y. J. Zhao, Q. Y. Wu, H. D. Nie, H. L. Si, H. Huang, Y. Liu, M. W. Shao and Z. H. Kang, *Nano Res.*, 2022, **15**, 4000–4007.
- 25 S. S. Mondal, S. R. Das, L. Sahoo, S. Dutta and U. Gautam, *J. Am. Chem. Soc.*, 2022, **144**, 2580–2589.
- 26 Q. Li, S. C. Wang, Z. X. Sun, Q. J. Tang, Y. Q. Liu, L. Z. Wang, H. Q. Wang and Z. B. Wu, *Nano Res.*, 2019, **12**, 2749–2759.
- 27 X. Q. Gu, Z. M. Chen, Y. Li, J. Wu, X. Wang, H. Huang, Y. Liu, B. Dong, M. W. Shao and Z. H. Kang, *ACS Appl. Mater. Interfaces*, 2021, **13**, 24814–24823.
- 28 Z. Z. Su, B. X. Zhang, J. B. Shi, D. X. Tan, F. Y. Zhang, L. F. Liu, X. N. Tan, D. Shao, G. Y. Yang and J. L. Zhang, *Sustain. Energy Fuels*, 2019, **3**, 1233–1238.
- 29 X. W. Shi, C. Dai, X. Wang, J. Y. Hu, J. Y. Zhang, L. X. Zheng, L. Mao, H. J. Zheng and M. S. Zhu, *Nat. Commun.*, 2022, **13**, 1287.
- 30 Q. Cheng, Y. J. Yuan, R. Tang, Q. Y. Liu, L. Bao, P. Wang, J. S. Zhong, Z. Y. Zhao, Z. T. Yu and Z. G. Zou, *ACS Catal.*, 2022, **12**, 2118–2125.
- 31 Q. Liang, X. T. Yan, Z. Y. Li, Z. Y. Wu, H. Shi, H. Huang and Z. H. Kang, *J. Mater. Chem. A*, 2022, **10**, 4279–4287.
- 32 Y. Lu, W. J. Yin, K. L. Peng, K. Wang, Q. Hu, A. Selloni, F. R. Chen, L. M. Liu and M. L. Sui, *Nat. Commun.*, 2018, **9**, 2752.

- 33 C. Peng, T. Zhou, P. Wei, H. Q. Ai, B. P. Zhou, H. Pan, W. K. Xu, J. B. Jia, K. Zhang, H. J. Wang and H. Yu, *Chem. Eng. J.*, 2022, **439**, 135685.
- 34 Q. Liang, S. Zhao, Z. Y. Li, Z. Y. Wu, H. Shi, H. Huang and Z. H. Kang, *ACS Appl. Mater. Interfaces*, 2021, **13**, 40754–40765.
- 35 Y. X. Wang, Y. Y. Zhang, X. J. Zhu, Y. Liu and Z. B. Wu, *Appl. Catal., B*, 2022, **316**, 121610.
- 36 X. X. Zhang, Y. G. Xiao, S. S. Cao, Z. L. Yin and Z. Q. Liu, *J. Clean. Prod.*, 2022, **352**, 131560.
- 37 Y. J. Bai, X. B. Yi, B. Li, S. W. Chen and Z. J. Fan, *Appl. Surf. Sci.*, 2022, **578**, 151993.
- 38 Z. Man, Y. Meng, X. C. Lin, X. R. Dai, L. P. Wang and D. Z. Liu, *Chem. Eng. J.*, 2022, **431**, 133952.
- 39 G. L. Mo, L. X. Wang and J. H. Luo, *Sep. Purif. Technol.*, 2021, **277**, 119643.
- 40 Z. G. Yin, T. T. Song, W. T. Zhou, Z. L. Wang and Y. Ma, *J. Catal.*, 2021, **402**, 289–299.
- 41 K. M. Kamal, R. Narayan, N. Chandran, S. Popović, M. A. Nazrulla, J. Kovač, N. Vrtovec, M. Bele, N. Hodnik, M. M. Kržmanc and B. Likozar, *Appl. Catal., B*, 2022, **307**, 121181.
- 42 X. M. Cheng, X. Y. Dao, S. Q. Wang, J. Zhao and W. Y. Sun, *ACS Catal.*, 2021, **11**, 650–658.
- 43 Y. Chen, G. B. Mao, Y. W. Tang, H. Wu, G. Wang, L. Zhang and Q. Liu, *Chin. J. Catal.*, 2021, **42**, 225–234.
- 44 X. D. Zhang, K. Yue, R. Z. Rao, J. F. Chen, Q. Liu, Y. Yang, F. K. Bi, Y. X. Wang, J. C. Xu and N. Liu, *Appl. Catal., B*, 2022, **310**, 121300.
- 45 L. B. Wang, B. Chen, L. Y. Zhang and J. G. Yu, *Small*, 2021, **17**, 2103447.
- 46 S. H. Wu, X. F. Xing, D. Wang, J. Z. Zhang, J. M. Chu, C. C. Yu, Z. T. Wei, M. L. Hu, X. Zhang and Z. X. Li, *ACS Sustain. Chem. Eng.*, 2020, **8**, 148–153.
- 47 X. J. Yang, H. W. Sun, G. Y. Li, T. C. An and W. Choi, *Appl. Catal., B*, 2021, **294**, 120252.
- 48 X. J. Li, K. Y. Zhang, X. B. Huang, Z. Y. Wu, D. F. Zhao and G. Wang, *Nanoscale*, 2021, **13**, 19671–19681.
- 49 S. Q. Zhang, X. Liu, C. B. Liu, S. L. Luo, L. L. Wang, T. Ca, Y. X. Zeng, J. L. Yuan, W. Y. Dong, Y. Pei and Y. T. Liu, *ACS Nano*, 2018, **12**, 751–758.
- 50 K. Wang, X. H. Li, N. Wang, Q. H. Shen, M. C. Liu, J. C. Zhou and N. X. Li, *Ind. Eng. Chem. Res.*, 2021, **60**, 8720–8732.
- 51 P. She, B. Y. Guan, J. Y. Sheng, Y. Y. Qi, G. Y. Qiao, H. B. Rui, G. Y. Lu, J.-S. Qin and H. Rao, *Catal. Sci. Technol.*, 2022, **12**, 1092–1099.
- 52 H. H. Li, F. Zhang, H. F. Wang, J. R. Xue, Y. M. Guo, Q. Z. Qian and G. Q. Zhang, *Energy Environ. Sci.*, 2021, **14**, 5339–5346.
- 53 C. H. Liu, Y. H. Yao, L. Sun, L. L. Luo, W. C. Wang and Z. D. Chen, *Chem. Commun.*, 2021, **57**, 9846–9849.
- 54 A. R. Amani-Ghadim, F. Khodam and M. S. Dorraji, *J. Mater. Chem. A*, 2019, **7**, 11408–11422.
- 55 T. Wang, Q. Y. Men, X. Q. Liu, H. Q. Zhan and Y. Q. Wang, *Sep. Purif. Technol.*, 2022, **294**, 121215.
- 56 X. H. Ma, D. Y. Li, Y. H. Jiang, H. C. Jin, L. Y. Bai, J. Qi, F. F. You and F. L. Yuan, *J. Colloid Interface Sci.*, 2022, **628**, 768–776.
- 57 Y. Li, Y. Zhao, J. Wu, Y. D. Han, H. Huang, Y. Liu and Z. H. Kang, *J. Mater. Chem. A*, 2021, **9**, 25453–25462.
- 58 Y. X. Li, Y. X. Liu, X. Liu, Y. L. Liu, Y. Y. Cheng, P. Zhang, P. J. Deng, J. J. Deng, Z. H. Kang and H. T. Li, *Nano Res.*, 2022, **15**, 6026–6035.
- 59 J. Z. Zhao, M. X. Ji, H. L. Chen, Y.-X. Weng, J. Zhong, Y. J. Li, S. Y. Wang, Z. R. Chen, J. X. Xia and H. M. Li, *Appl. Catal., B*, 2022, **307**, 121162.
- 60 Y. Ke, Q. Liang, S. Zhao, Z. H. Zhang, X. Z. Li and Z. Y. Li, *Inorg. Chem.*, 2022, **61**, 2652–2661.
- 61 J. X. Xu, Y. F. Chen, M. Chen, J. Wang and L. Wang, *Chem. Eng. J.*, 2022, **442**, 136208.
- 62 P. Verma, F. A. Rahimi, D. Samanta, A. Kundu, J. Dasgupta and T. K. Maji, *Angew. Chem., Int. Ed.*, 2022, **61**, e202116094.
- 63 G. M. Ren, S. T. Liu, Z. Z. Li, H. C. Bai, X. D. Hu and X. C. Meng, *Sol. RRL*, 2022, **6**, 2200154.
- 64 L. B. Wang, B. Cheng, L. Y. Zhang and J. G. Yu, *Small*, 2021, **17**, 2103447.
- 65 B. X. Ni, H. Jiang, W. Y. Guo, Q. J. Xu and Y. L. Min, *Appl. Catal., B*, 2022, **307**, 121141.
- 66 Z. R. Miao, Q. L. Wang, Y. F. Zhang, L. P. Meng and X. X. Wang, *Appl. Catal., B*, 2022, **301**, 120802.
- 67 Y. J. Ma, Q. Tang, W. Y. Sun, Z. Y. Yao, W. H. Zhu, T. Li and J. Y. Wang, *Appl. Catal., B*, 2020, **270**, 118856.